Proceedings of the ASME 2019
International Design Engineering Technical Conferences
and Computers and Information in Engineering Conference
IDETC/CIE2019
August 18-21, 2019, Anaheim, CA, USA

DETC2019-97136

DYNAMICS ANALYSIS OF THE DEPLOYMENT OF MIURA-ORIGAMI SHEETS

Yutong Xia[1], Kon-Well Wang[1]
[1]Department of Mechanical Engineering,
University of Michigan, Ann Arbor, MI, USA 48109

ABSTRACT

Origami has emerged as a promising tool for the design of mechanical structures that can be folded into small volume and expanded to large structures, which enables the desirable features of compact storage and effective deployment. Most attention to date on origami deployment has been on its geometry, kinematics, and quasi-static mechanics, while the dynamics of deployment has not been systematically studied. On the other hand, deployment dynamics could be important in many applications, especially in high speed operation and low damping conditions. This research investigates the dynamic characteristics of the deploying process of origami structures through investigating a Miura-Ori sheet (Fig. 1(b, c)). In this study, we have utilized the stored energy in pre-deformed spring elements to actuate the deployment. We theoretically model and numerically analyze the deploying process of the origami sheet. Specifically, the sheet is modeled by bar-and-hinge blocks, in which the facet and crease stiffnesses are modeled to be related to the bar axial deformation and torsional motion at the creases. On the other hand, the structural inertia is modelled as mass points assigned at hinges. Numerical simulations show that, apart from axial contraction and expansion, the origami structure can exhibit transverse motion during the deploying process. Further investigation reveals that the transverse motion has close relationship with the controlled deploying rate. This research will pave the way for further analysis and applications of the dynamics of origami-based structures.

Keywords: Origami, deployment, dynamics, deployable.

1. INTRODUCTION

Origami, an ancient paper folding art, has gained new life recently, as its principles have not only been explored in mathematics and aesthetics, but also shed light on design and manufacturing of engineering structures with profuse functionalities. There have been many applications explored since the 20th century, which take advantage of the idea that an origami-based structure can be folded into small volume and subsequently deployed into 3D structures, for example, reconfigurable architectural façade [1] and foldable space structures [2]. Additionally, origami has also demonstrated its value in the development of mechanical and material systems with extraordinary properties originating from folding, such as reprogrammable stiffness [3], locking and stiffness jump [4], and multi-stability [5]. Despite the research progress on the static and quasi static characteristics of origami, the study on origami dynamics is limited. On one hand, these origami structures could subject to dynamic load from the environment, thus it is necessary to understand their dynamic behavior for safety concerns and better controls [6], where previous studies have shown the ability of origami structures in noise mitigation [7] and vibration isolation [8]. On the other hand, the dynamics of origami deployment has not been explored. Therefore, to advance the state of art, the goal of this paper is to investigate the dynamics characteristics of origami deploying process and build a rigorous and comprehensive framework for exploring origami dynamic behaviors.

In this research, we focus our effort on the deployment dynamics of a Miura-Ori sheet. Miura-Ori is a widely used origami pattern design (Fig. 1(a)) and can achieve flat-foldability. A Miura-Ori sheet can be constructed by connecting the Miura-Ori cells repeatedly along their creases (Fig. 1(b, c)). Various actuation methods have been designed and explored for deployable structures [9], [10], including pneumatic actuation [11], stored energy [12], and thermal activation with shape memory materials [13]. For the purpose of easy illustration without losing generosity, we have been utilizing the stored energy method in this study. Instead of assuming rigid folding, we build our dynamic model with the bar and hinge model [14], [15]. The panel facet is represented by a N5B8 model (Fig. 1(d)), with which the facet could exhibit shear and bending deformation, thus large transverse motions can be captured during the deployment process. Mass point is assigned at the

---

[1] Contact author: yutoxia@umich.com

position of hinges with appropriate values to simulate facet inertia.

Numerical simulations reveal rich dynamics that has never been reported. In the case of free deployment driven by stored energy, time-varying transverse displacement is observed after fully deployed. In the displacement control case, where the structure's free end is controlled to move with prescribed speed, different types of transverse motions are observed with different deploying rate. Flapping motion shows up after structure being fully deployed. Further analysis shows the relationship between the intensity of the transverse motion and the deploying rate. This paper is organized as follows. Section 2 introduces the dynamic modeling of a Miura-Ori sheet. Section 3 presents the numerical analysis of the free deployment driven by stored energy. Section 4 presents numerical analysis of the displacement-controlled deployments. A brief summary and discussion is presented in Section 5.

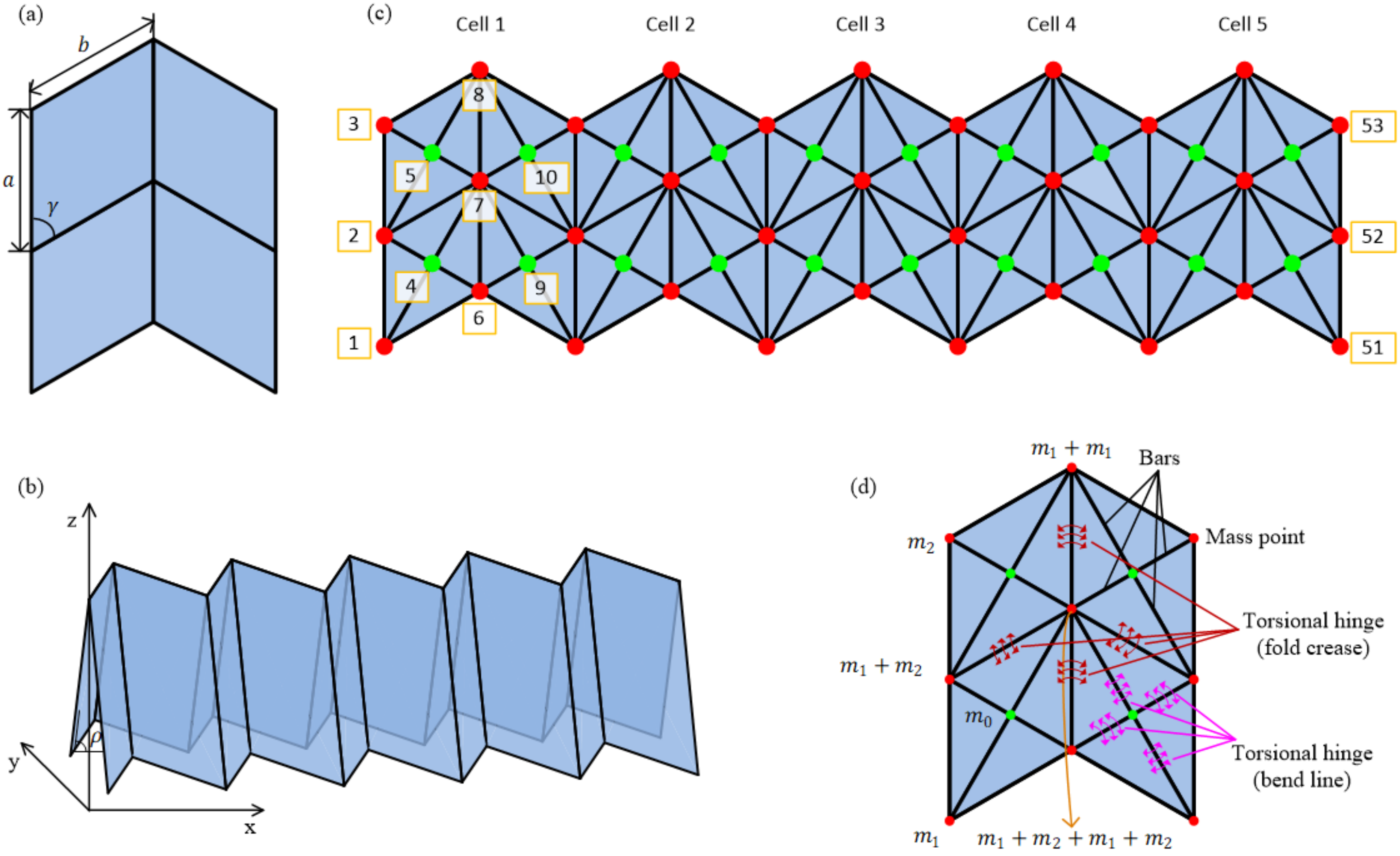

Figure 1. 1(a) shows the Miura-Ori cell, and the geometry parameters (a, b, γ) can be found here. 1(b) shows the rigid folded configuration of the Miura-Ori cell with folding angle $\rho = 80°$. The coordinate used in this paper can be found here. 1(c) shows the Miura-Ori sheet constructed by connecting five identical Miura-Ori cells along the creases. The node numbering is also shown here. Details of the embedded bar-and-hinge model in each Miura-Ori cell are depicted in 1(d). The N5B8 model consists of eight bars and five nodes. The nodes in green and red represent the mass points in the center and at vertices respectively. Mass point m_0 is assigned at the position of the center node; m_1 at the vertices of long diagonal; m_2 at the vertices of short diagonal. The four lines inside each parallelogram are the massless bars and are attached with hinge springs representing fold creases and bend lines.

2. DYNAMIC MODELING FOR ORIGAMI DEPLOYMENT

2.1 Geometry of Miura-Ori Sheet

The Miura-Ori sheet is formed by connecting Miura-Ori cells head-to-tail along their creases (Fig. 1(b, c)). In this work, the sheet contains five Miura-Ori cells. Miura-Ori is a degree-4 vertex pattern with a pair of collinear creases and reflection symmetry about these creases. Each Miura-Ori cell consists of four identical parallelograms and can be described by three parameters: the length of adjacent creases (a, b), and the section angle γ between them. A rigid Miura-Ori cell possesses single degree of freedom (DOF), and can be described by the dihedral angle ρ. If assume rigid, the integrated Miura-Ori sheet has single DOF, and all cells share the same dihedral angle. In this work, we use ρ to describe the structure configuration when there is no facet deformation.

2.2 Stiffness of Miura-Ori Sheet

In this research, we use the bar-and-hinge model to describe the elastic behavior of the Miura-Ori sheet [14], [15]. Such behavior is a combined result of the in-plane deformation of panel facets, the bending of panels, and the folding along the fold creases. Each parallelogram in the Miura-Ori cells is replaced with an N5B8 model, one of the bar-and-hinge models and the node numbering is as shown in Fig. 1(c). Assumptions made in this bar-and-hinge model are: (a) a straight fold line between surfaces remains straight after adjacent material deforms, and (b) a triangular face remains planar while the quadrilateral face exhibits bending along its diagonals, local effect around the boundary neglected. With this model, (i) the in-plane stiffness is represented by bar elements with axial stiffness, which simulates the shear and stretching behavior of thin panel facet, (ii) the out-of-plane bending stiffness of flat panel facets is represented by torsional hinges around diagonal bars, which simulates the facet bending motion, and (iii) the bending stiffness along fold creases is represented by rotational hinges around fold creases, which simulates the intended bending for kinematic folding of origami structures.

For a parallelogram panel facet, its important parameters include the section angle γ, short diagonal length D_S, thickness t, and material constants Young's modulus E and Poisson's ratio ν. Eq. (1-2) shows the relationship between the bending angle θ_B and the torque M_B at the bending line, while M_{BS} deals with small angular deformation, and M_{BL} deals with large angular deformation [15]. As the stiffness ratio between fold and bend creases K_B/K_F falls in range $[1/3, 20]$, this model would provide realistic estimate of structure behaviors. These equations will provide reasonable approximation for stiffness parameters in dynamic modeling.

$$M_{BS} = \theta_B\left(0.55 - 0.42\frac{2\gamma}{\pi}\right)\frac{Et^3}{12(1-\nu^2)}\left(\frac{D_S}{t}\right)^{1/3} \tag{1}$$

$$M_{BL} = \theta_B^{4/3}\frac{Et^3}{12(1-\nu^2)}\left(\frac{D_S}{t}\right)^{1/3} \tag{2}$$

2.3 Inertia of Miura-Ori sheet

A finite DOF model is applied to simplify the analysis of origami structures. The continuum panel facet is represented by an assemblage of mass points located at the positions of five nodes. This method could provide a simple and effective way to simulate the inertia origami structures.

We first derive the moment of inertia of the parallelogram continuum and the mass-point assemblage. There are three kinds of mass point $[m_0, m_1, m_2]$. m_0 is located in the center of the panel facet, m_1 is located on the long diagonal axis, and m_2 is along the short diagonal. The total mass of these mass points is kept the same as the mass of facet panel. The two independent variables $[m_1, m_2]$ are determined by minimizing the error of moment of inertia between facet panel and the mass point assemblage. The principal moments of inertia of a parallelogram continuum are as shown in Eqs. (3-5). S is the panel area. Eq. (6) shows the moment of inertia of a mass point with relative position r. The error between inertia components is depicted in Fig. 2. By selecting the mass points $[m_1, m_2]$ to be [0.25, 0.028] (total mass is 1), the errors in the three principal directions are $[0.8\%, 0, 0.2\%]$, which are reasonably small. When assemble the overall inertia matrix, there will be two or four mass points located at the same nodal position at connecting lines (Fig. 1(d)). Therefore, we could simulate the translational and rotational inertia of the Miura-Ori sheet.

$$I_1 = \frac{m}{24}\left(a^2 + b^2 - \sqrt{(a^2+b^2)^2 - 4S^2}\right) \tag{3}$$

$$I_2 = \frac{m}{24}\left(a^2 + b^2 + \sqrt{(a^2+b^2)^2 - 4S^2}\right) \tag{4}$$

$$I_3 = \frac{m}{12}(a^2 + b^2) \tag{5}$$

$$I = m(|r|^2 - rr^T) \tag{6}$$

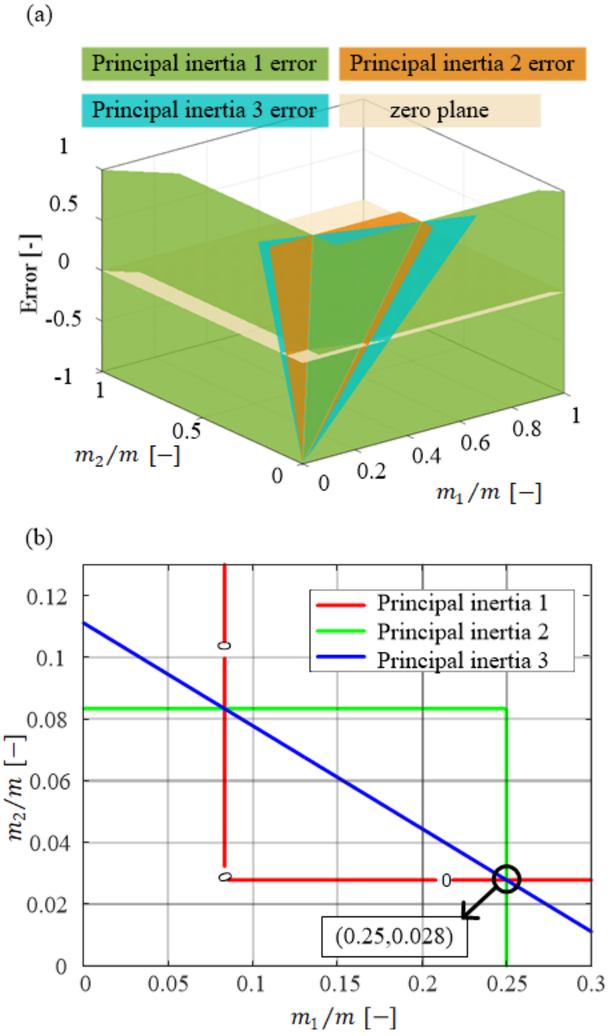

Figure 2. The error of the principal moments of inertia between continuum parallelogram and assemblage of mass points $(I_{mass\,points} - I_{true})/I_{true}$. 2(a) shows the 3D plot of the errors. 2(b) shows the contour lines of zero error.

2.4 Dynamic Modeling of the Miura-Ori Sheet

The equivalent dynamic model of the Miura-Ori sheet consists of mass points constrained by massless bars and massless torsional hinges. Each node has three DOFs, and the generalized coordinates are the linear displacements of nodes. Thus, the kinetic energy is as shown in Eq. (7).

$$T = \frac{1}{2} m_i \dot{r}_i^{\,2} \tag{7}$$

Each bar in the model can be denoted by the numbering of its two ending nodes. The strain energy can be derived from the axial deformation as Eq. (8). $W(S_{GL})$ is the strain energy density function as in Eq. (9), and S_{GL} is the Green-Lagrange strain tensor. μ_i, α_i, N are material constants, and λ_1 is the axial stretch.

$$U_{bar} = \int_0^{L_{bar}} W(S_{GL}) A_{bar} dx \tag{8}$$

$$W(S_{GL}) = \sum_{i=1}^{N} \frac{\mu_i}{\alpha_i} (\lambda_1^{\alpha_i} - 1) \tag{9}$$

$$\lambda_1 = \sqrt{2S_{GL} + 1} \tag{10}$$

The potential energy from the torsional hinges is as shown in Eq. (11). The bending angle θ is determined by its two adjacent triangles, or equivalently four nodes. Eq. (12) shows the i-th nodal force. This nodal force is generated from the hinge torque at one of the creases connected to this node. Details about the relationship between the bending angle θ and its four dependent nodal displacements x can be found in [14]. Thus the final i-th nodal force is derived by traverse of all creases connected to this node and summing up the corresponding nodal forces with Eq. (12).

$$V_{crease} = \int_{\theta_0}^{\theta} M(\hat{\theta}) d\hat{\theta} \tag{11}$$

$$F_{crease,i} = \frac{\partial V_{crease}}{\partial x_i} = \frac{\partial V_{crease}}{\partial \theta} \frac{\partial \theta}{\partial x_i} = M(\theta) \frac{\partial \theta}{\partial x_i} \tag{12}$$

Dissipation comes from bar deformation, as well as fold and bend creases. At the hinges it has the form shown in Eq. (13).

$$\begin{gathered} F_{d,crease,i} = \frac{\partial D_{crease}}{\partial \dot{x}_i} = C\dot{\theta} \frac{\partial \dot{\theta}}{\partial \dot{x}_i} \\ \frac{d}{dt}\theta(x) = \frac{d\theta}{dx_i} \frac{dx_i}{dt} \end{gathered} \tag{13}$$

By using the Lagrange's equations, we could assemble the equations of motion (EOMs) with respect to each nodal linear displacement x.

$$\begin{gathered} L = T - (U_{bar} + V_{crease}), \\ \frac{d}{dt}\left(\frac{\partial L}{\partial \dot{x}_i}\right) - \frac{\partial L}{\partial x_i} + \frac{\partial D}{\partial \dot{x}_i} = 0. \end{gathered} \tag{14}$$

In the numerical simulations, the Young's modulus takes on value as $2e11\ [N/m^2]$; dissipation as $0.1\ [N \cdot m \cdot sec]$ at fold creases, and $1\ [N \cdot m \cdot sec]$ at bend creases; mass as $3\ [kg]$ for each panel.

Two kinds of boundary conditions are applied to evaluate the deploying behavior of the Miura-Ori sheet. On the left end, the middle node is fixed in space, and the x direction motion of the two side nodes are constrained (coordinate system shown in Fig. 1(b)). In this way, the left end creases have fixed position and orientation while keeping the flexibility to deploy. On the right end, the middle node is constrained in the y, z direction with a roller support, thus it can only move along the axial direction. In the free deployment case, the middle point can freely move in the x direction. For a displacement control case, all three nodes on the right end is controlled to move with prescribed speed along the axial direction, while the middle node is fixed in the y and z directions. Once the structure reaches the flat-deployed configuration, the displacement control will keep the middle node at that position. In Tables 1 and 2, we denote 1 to the DOF if there are constraints and 0 if it is not constrained or controlled

EOMs without boundary conditions are first derived, and thus contain rigid motion DOFs. As for the constrained or controlled DOF, the generalized coordinate is replaced by its given position (if fixed) or time-varying position (if displacement controlled), and then the equation corresponding to this DOF is deleted from the overall EOMs.

Table 1. Constraints in case 1

Node No.	X	Y	Z
1	1	0	0
2	1	1	1
3	1	0	0
51	0	0	0
52	0	1	1
53	0	0	0

Table 2. Constraints in case 2

Node No.	X	Y	Z
1	1	0	0
2	1	1	1
3	1	0	0
51	Displacement control	0	0
52	Displacement control	1	1
53	Displacement control	0	0

3. DYNAMIC ANALYSIS OF DISPLACEMENT-CONTROLLED DEPLOYMENT

We first examine the deploying behavior of the Miura-Ori sheet with displacement control. The stress-free state of this Miura-Ori is the deployed state. The Miura-Ori sheet is bounded into a compressed state with $\rho = 80^\circ$ at the beginning. At this stage, it is rigidly folded and there is no panel facet deformation, but the torsional springs at the crease will be deformed and contain potential energy used to activate the deployment.

As it starts to deploy, the bounding mechanism is released and the displacement control on the right end starts. Apart from the single DOF motion based on rigid folding assumption, this Miura-Ori sheet could have transverse motions. The first kind of transverse motion being observed is in the xy plane. With different deploying displacement control rates, there exist different types of transverse motion. In the case of rate $a/5$ $[m/sec]$ (a is the side length of the Miura-Ori panel as shown in Fig. 1(a)), the rightmost cell deploys first, leaving the rest of the cells limited expansion space. The structure contains high level of potential energy at this stage, thus it tends to have out-of-plane motion out from the xz plane (Fig. 3(c)) because of the relatively lower bending stiffness than in other directions[15]. The deploying sequence of cells in the Miura-Ori sheet can be found from the folding angles in Fig. 3(b). As the deployment continues, the global bending motion can be observed in the xz plane as well as the time-varying transverse displacement along the structure. After all the cells are deployed, the flapping motion starts inside each cell. This is caused by oscillations in the folding and bending angle. In the case of slower deploying rate as $a/50$, the deploying sequence changes, as the center cell deploys first. Such slow rate allows time for interaction among all the cells, thus the structure exhibits an almost symmetric configuration during deployment, as can be seen in Fig. 3(f).

We expand our study to understand the effect of deploying rate on the structural dynamic behaviors. We explore 11 different deploying rates, ranging in $[a/50, a/40, a/30, a/20, a/10, a/5, a/2, 2a, 3a, 5a, 10a]$. We are mainly interested in two aspects in the dynamic behaviors, the facet bending and the motion range. Motion range, resulting from out-of-plane motion from xz plane at the early deploying stage and global bending at the late deploying stage, shows the deviation from the assumed rigid folding path. In Fig. 4(a), the motion range in the xy plane, resulting mainly from the out-of-plane motion from the xz plane, increases with the rate until $a/5$ and decreases ever since. This indicates that as deploying rate increases over $a/5$, from right to left, the Miura-Ori cells are stretched to deploy before interaction happens. Additionally, when the deploying rate is low enough, the Miura-Ori cells vibrate in a small range beyond its initial configuration, and settle down around the new configuration before large motion is triggered. However, one of the drawbacks of fast deployment is that it would cause more panel facet deformation as shown in Fig. 4(b). Such bending grows rapidly as deploying rate increases over $a/5$.

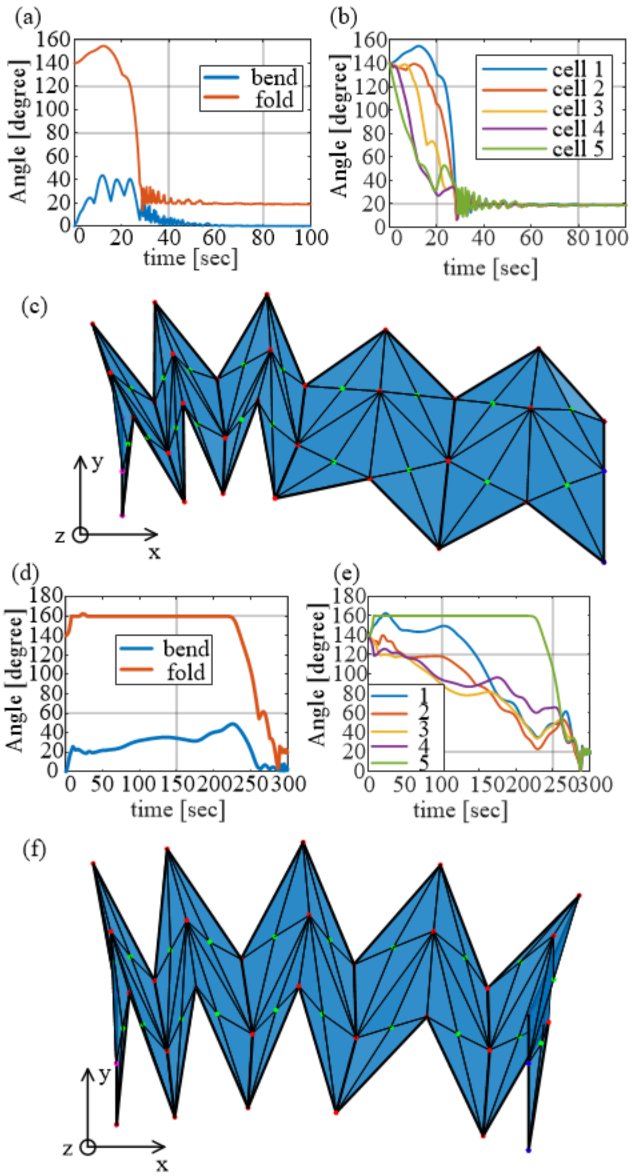

Figure 3. Plots (a-c) show the deployment with displacement control rate as $a/5$, and plots (d-f) correspond to rate $a/50$. 3(a) and 3(d) show the maximum angular displacement throughout deployment at bending and folding lines. 3(b) and 3(e) show the maximum folding angle of the five cells inside the Miura-Ori sheet, which indicates the deploying sequence. It can be seen that in the $a/5$ case, the deploying sequence is from right to left, and in the $a/50$ case, it is from center to periphery. 3(c) shows the top view of configuration at 10 sec during deployment, where there is out-of-plane motion out from the xz plane of the left three cells. 3(f) shows the configuration at 12 sec, where the center cells deploy first and exhibits rough symmetry.

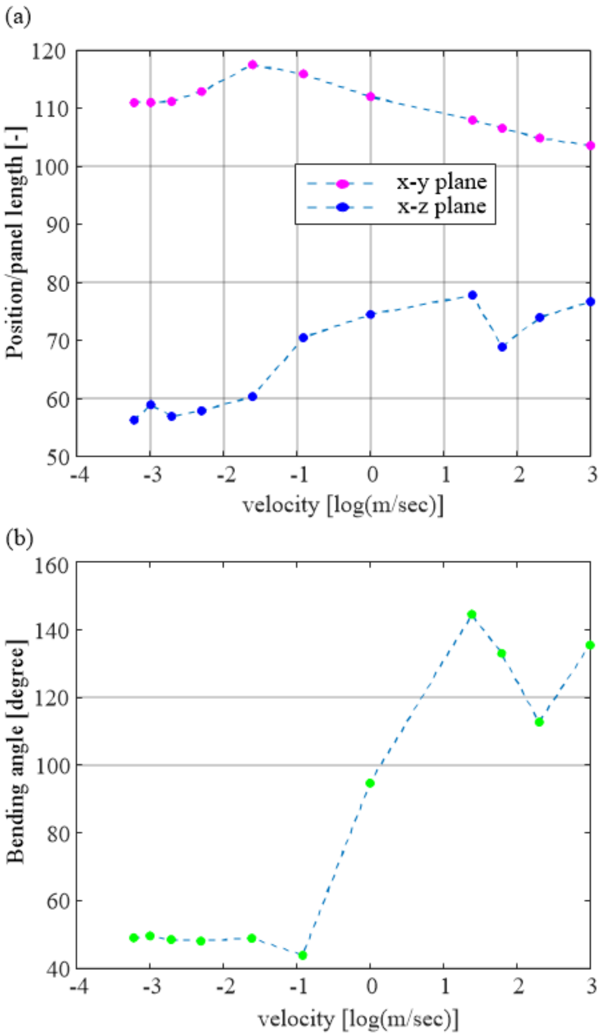

Figure 4. 4(a) shows the max positions reached in the xy and xz plane respectively throughout the deployment process, scaled with respect to the facet size a. The facet bending is shown in 4(b), which consists of elastic deformation of the panel facets.

4. DYNAMIC ANALYSIS OF FREE DEPLOYMENT BY STORED ENERGY

To better understand the dynamics of Miura-Ori deployment, we also investigate the free deployment process. Similarly, the Miura-Ori sheet starts from the folded state with $\rho = 80°$ with stress-free state as the deployed state. When the Miura-Ori is set free, the stored potential energy drives the structure to deploy. The deployment starts from the rightmost cell to the left end, similar to the $a/5$ case with displacement control. In this case, the Miura-Ori sheet starts to have global bending in the xz plane, as depicted in Fig. 5(b-f).

Fig. 5(a) shows that the axial velocity of the middle node on the right end increases as the deployment begins. It drops to zero when the structure first reaches the deployed state and then the global bending begins. The average speed before the deployed state is $0.48\ [m/sec]$. In the previous section, the case $a/5$ is close to this average velocity. This could provide insight into the change of behavior with deploying rate. When the deploying rate is close to the free deploying rate, there would be less out-of-plane motion among cells from the xz plane than slower rates. When the deploying rate becomes faster, the displacement control has a pulling and stretching effect on Miura-Ori cells, thus facet deformation becomes more significant. This indicates the possible design strategy of displacement control for desirable deployment paths of origami structures.

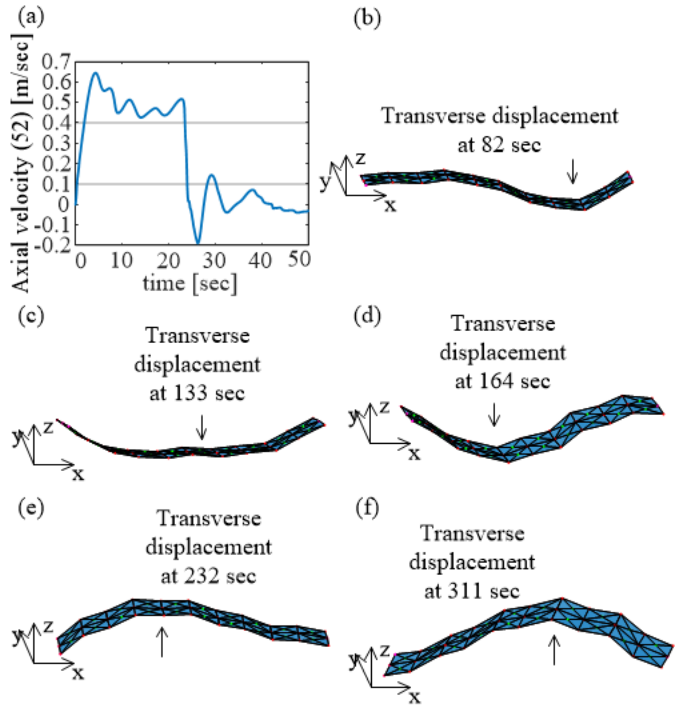

Figure 5. 5(a) shows the time-varying axial velocity of the middle node on the right end. 5(b-f) show the global bending varying with time after deployment.

5. CONCLUSION AND DISCUSSION

This study focuses on the dynamic behaviors of a Miura-Ori sheet deploying actuated by stored strain energy. Instead of quasi-static rigid-folding, facet elasticity and inertial effects are considered in this study and a dynamic model is established with bar-and-hinge elements as building blocks. The model is then analyzed via numerical simulations and multiple deploying configurations are observed under different deployment rates. Analyzing the free deployment case provides better understanding of the relationship between the origami dynamic behavior and the deploying rate. This study provides the foundation for exploring dynamic characteristics of the deployment of origami structures.

ACKNOWLEDGMENTS

This research was partially supported by the National Science Foundation under Award 1634545 and the University of Michigan Collegiate Professorship.

REFERENCES

[1] A. E. Del Grosso and P. Basso, “Adaptive building skin structures,” *Smart Mater. Struct.*, vol. 19, no. 12, 2010.

[2] K. Miura, “Method of packaging and deployment of large membranes in space,” *The Institute of Space and Astronautical Science report*, vol. 618. pp. 1–9, 1985.

[3] J. L. Silverberg *et al.*, “Using origami design principles to fold reprogrammable mechanical metamaterials,” *Science (80-.).*, vol. 345, no. 6197, pp. 647–650, 2014.

[4] H. Fang, S. C. A. Chu, Y. Xia, and K. W. Wang, “Programmable self-locking origami mechanical metamaterials,” *Adv. Mater.*, vol. 30, no. 15, pp. 1–9, 2018.

[5] H. Fang, K. W. Wang, and S. Li, “Asymmetric energy barrier and static diode effect from folding,” *Extreme Mechanics Letters*, no. 864, pp. 1–25, 2017.

[6] G. V. Rodrigues, L. M. Fonseca, M. A. Savi, and A. Paiva, “Nonlinear dynamics of an adaptive origami-stent system,” *Int. J. Mech. Sci.*, vol. 133, pp. 303–318, 2017.

[7] M. Thota and K. W. Wang, “Reconfigurable origami sonic barriers with tunable bandgaps for traffic noise mitigation,” *J. Appl. Phys.*, vol. 122, no. 15, 2017.

[8] K. Inamoto and S. Ishida, “Improved feasible load range and its effect on the frequency response of origami-inspired vibration isolators with quasi-zero-stiffness characteristics [1],” *J. Vib. Acoust.*, vol. 141, no. 2, p. 021004, 2018.

[9] S. A. Zirbel, B. P. Trease, S. P. Magleby, and L. L. Howell, “Deployment methods for an origami-inspired rigid-foldable array,” *Proc. 40th Aerosp. Mech. Symp.*, vol. NASA Godda, pp. 189–194, 2014.

[10] E. A. Peraza-Hernandez, D. J. Hartl, R. J. Malak, and D. C. Lagoudas, “Origami-inspired active structures: A synthesis and review,” *Smart Mater. Struct.*, vol. 23, no. 9, 2014.

[11] S. Li, H. Fang, and K. W. Wang, “Recoverable and programmable collapse from folding pressurized origami cellular solids,” *Phys. Rev. Lett.*, vol. 117, no. 11, pp. 1–5, 2016.

[12] T. Neilsen, C. Weston, C. Fish, and B. Bingham, “DICE: Challenges of spinning cubesats,” *Adv. Astronaut. Sci.*, vol. 151, pp. 387–403, 2014.

[13] A. J. Taylor *et al.*, “MR conditional SMA-based origami joint,” *IEEE/ASME Trans. Mechatronics*, vol. 4435, no. 617, pp. 1–1, 2019.

[14] K. Liu and G. H. Paulino, “Nonlinear mechanics of non-rigid origami : an efficient computational approach,” *Proc. R. Soc. A* 473: 20170348.

[15] E. T. Filipov, K. Liu, T. Tachi, M. Schenk, and G. H. Paulino, “Bar and hinge models for scalable analysis of origami,” *Int. J. Solids Struct.*, vol. 124, pp. 26–45, 2017.